Hierarchical microsphere of MoNi porous nanosheets as electrocatalyst and cocatalyst for hydrogen evolution reaction

Linjing Yang[a], Lili Zeng[a], Hui Liu[a], Yunqie Deng[a], Ziqian Zhou[a], Jiayuan Yu[a], Hong Liu[b,c,*], Weijia Zhou[a,b,*]

[a] *Guangzhou Key Laboratory for Surface Chemistry of Energy Materials, New Energy Research Institute, School of Environment and Energy, South China University of Technology, Guangzhou Higher Education Mega Center, Guangzhou, Guangdong, 510006, PR China*
[b] *Institute for Advanced Interdisciplinary Research, University of Jinan, Jinan, 250022, PR China*
[c] *State Key Laboratory of Crystal Materials, Center of Bio & Micro/Nano Functional Materials, Shandong University, 27 Shandanan Road, Jinan, Shandong, 250100, PR China*

ABSTRACT

In industrial water electrolysis cell, the electrocatalyst has a sluggish water dissociation kinetics leading to low electrocatalytic activity for the generation of H_2 from water splitting. This work reports a hierarchical microsphere constructed by MoNi porous nanosheets derived from $NiMoO_4$ microsphere, as a rapid Tafel-step-decided electrocatalyst towards hydrogen evolution reaction (HER). Consequently, the synthesized MoNi hierarchical microsphere (MoNi HM) electrocatalyst exhibits an onset potential of as small as −7 mV vs. RHE, an operating potential of 72 mV for 10 mA cm^{-2}, and a low Tafel slope of 36.6 mV per decade in 1.0 M KOH. Furthermore, MoNi HM as cocatalyst and CdS nanowires as photocatalyst are physically mixed (MoNi HM/CdS NWs) and presentes a champion photocatalytic performance for H_2 production with a prominent H_2 generation rate of as high as 151.7 μmol mg^{-1} h^{-1} at λ > 420 nm light illumination. The large contact area between MoNi nanosheets and CdS nanowires endows the fast separation of photogenerated charge carriers to significantly facilitate the photocatalytic H_2 production.

1. Introduction

With respect to the challenges of global energy crisis and environmental concerns, it's necessary to develop alternate energy approaches for natural fossil energy, such as, sustainable hydrogen generated through a green and efficient way of water electrolysis [1–5]. The most efficient electrocatalysts towards hydrogen evolution reaction (HER) are Pt-group metals as they can dramatically reduce overpotential and speed up the kinetics for driving HER [6–8]. Nevertheless, large-scale commercial H_2 generation was limited by the high cost of Pt based electrocatalysts [9]. The earth-abundant non-Pt electrocatalysts, such as transition-metal chalcogenides [4,10–12], oxide [13,14], phosphide [15], carbides [4,16,17], and carbon based electrocatalysts [5,18–20] recently have been intensively studied. Consequently, it is still urgent to investigate non-precious metal-based catalysts as suitable substitutes of Pt while desirable.

The suitable transition metal alloys were known electrocatalysts with superior HER electrocatalytic activity and durability for hydrogen production in alkaline electrolytes, such as nickel-molybdenum

[21–26]. I. A. Raj and co-workers researched various binary alloys catalysts towards HER and disclosed that the NiMo alloy displayed a low overpotential of about 40 mV [27,28]. Introducing Mo element to metallic Ni to form alloy could through revising d-band electronic density state to accommodate the surface free energy of hydrogen adsorption (ΔG_{H*}), which promoted ad-/desorption toward H process. Prof. Feng investigated a Ni foam supported $MoNi_4$ electrocatalyst anchored on MoO_2 cuboids ($MoNi_4/MoO_2@Ni$) by annealing $NiMoO_4$ cuboids precursor in a reduction atmosphere. The achieved $MoNi_4/MoO_2@Ni$ displayed a Pt-like catalytic activity (onset potential: 0 mV; Tafel slope: 30 mV dec^{-1}). Ni atom is established as outstanding H_2O dissociation centers, furthermore Mo atom possesses excellent hydrogen adsorption performance [29]. Therefore, MoNi-group alloy ($MoNi_x$) catalysts can be competing substitutes attributing to a largely lower the energy barrier towards the Volmer step and accelerate the sluggish kinetics of water-alkali electrolysis for hydrogen production. In order to discuss the intrinsic catalytic activity, the specific topographic structure of $MoNi_x$ alloy should be established and the congruent relationship between above parameter and electrocatalytic activity

should be studied.

In addition, highly active electrocatalysts, such as noble metals [30] and non-precious metals of MoS$_2$ [31–35], MoP [36], Ni$_{12}$P$_5$ [37,38], NiCoB [39], Ni–Mo [40] and Ni$_3$C [41] used as the cocatalysts for photocatalytic hydrogen production were widely reported because the electronic structure of those cocatalysts facilitate the decomposition of water to H$_2$ with a low kinetic activation barrier [42,43]. For instance, Prof. Yang investigated that amorphous transition-metal borides (TMBs) of NiCoB were extraordinary candidates for Pt-group cocatalysts and leaded to outstanding photocatalytic H$_2$ production via water-splitting. The hydrogen evolution rate for nanostructured NiCoB/CdS composites under visible light irradiation (λ > 400 nm) could be as high as 144.8 mmol h^{-1} g^{-1}, up to 36 times higher than that of CdS alone [39]. What's more, Wang et al. prepared the Ni-Mo alloys modified g-C$_3$N$_4$ photocatalysts showed obviously enhanced visible-light photocatalytic HER activity, which possessed an excellent hydrogen evolution rate of 1785 µmol g^{-1} h^{-1} [44]. However, the loading methods were complicated and the loading amounts of cocatalysts on photocatalyst were nonadjustable.

In this study, we reported uniform hierarchical microspheres composed of MoNi alloy porous nanosheets synthesized from NiMoO$_4$ at a reduction atmosphere and the phase transformation process was studied by in situ High-Temperature X-ray diffraction (HT-XRD) technology. The obtained MoNi hierarchical microsphere (MoNi HM) exhibited a superior HER activity with a small onset potential of -7 mV vs. RHE and a low Tafel slope of 36.6 mV dec^{-1} in 1.0 M KOH aqueous solution. In addition, the MoNi HM were used as cocatalyst for photocatalytic hydrogen production with rate of 151.7 µmol mg^{-1} h^{-1}, which only needed to be physically mixed with CdS nanowires.

2. Experimental

2.1. Materials

Mo powder (Mo), ammonium molybdate ((NH$_4$)$_6$Mo$_7$O$_{24}$·4H$_2$O), sodium molybdate (Na$_2$MoO$_4$), hydrogen peroxide (H$_2$O$_2$, 30% w/w), nickel (II) acetate (Ni(OAc)$_2$·4H$_2$O), urea (CO(NH$_2$)$_2$), sulfuric acid (H$_2$SO$_4$), potassium hydroxide (KOH), and 5 wt% Nafion solution were provided by Aladdin, cadmium acetate dihydrate (Cd(OAc)$_2$ ·2H$_2$O), sulfur powder (S), ethylenediamine (C$_2$H$_8$N$_2$), sodium sulfide non-ahydrate (Na$_2$S·9H$_2$O) and sodium sulfite (Na$_2$SO$_3$) were offered by Tianjin Guangfu Technology Development Company, commercial Pt/C (20 wt%) catalyst was obtained from Alfa Aesar. Deionized (D.I.) water was purified using a water purifier (Milli-Q, USA).

2.2. Synthesis of MoO$_3$ nanobelts (MoO$_3$ NBs)

Briefly, Mo powder (2.5 mmol) was added slack in H$_2$O$_2$ solution (2.0 mL) under vigorously magnetic stirring for 1 h in an ice-water bath to obtain a clarified yellow precursor dispersion containing the MoO$_2$(OH)(OOH), afterwards the introduction of D.I. water (12.5 mL) on-going stirring and further reaction for 6 h, a homogeneous solution was formed, and then was transferred into a Teflon-lined autoclave (20 mL), and maintained at 220 °C for 2 days. After cooling naturally, the precipitate of MoO$_3$ nanobelts (MoO$_3$ NBs) was isolated, washed with and ethanol three times in turn, and then dried in dry box at 65 °C for 12 h.

2.3. Preparation of NiMoO$_4$ microspheres (NiMoO$_4$ M)

1.0 mmol Ni(OAc)$_2$·4H$_2$O, 1.0 mmol MoO$_3$ NBs, and 4.0 mmol CO(NH$_2$)$_2$ were dispersed with 15 mL D.I. water into a 20 mL Teflon autoclave by ultrasound treatment, and then was heated at 160 °C for 10 h. After being cooled to room temperature, the NiMoO$_4$ microspheres were obtained by washing with D.I. water and be dried at 80 °C for 24 h.

2.4. Preparation of hierarchical microspheres of MoNi alloy porous nanosheets (MoNi HM)

The NiMoO$_4$ M was subjected the reducing treatment at 650 °C for 2 h under a H$_2$/Ar (v/v, 3/97) atmosphere and MoNi alloy hierarchical microspheres composed of porous nanosheets were synthesized. In addition, the pure Ni nanoparticles were obtained by the same procedure without adding MoO$_3$ NBs. As - a similar process without adding Ni(OAc)$_2$·4H$_2$O couldn't get precipitates, thus the contrast sample of pure Mo nanosheets was obtained [31]. At last, in order to survey the effect of reduction temperature, 450 °C, 550 °C, 750 °C, and 850 °C were also applied for the synthesis of MoNi alloy.

2.5. Preparation of CdS nanowires (CdS NWs) photocatalyst

CdS NWs was prepared according to literature [45]. Typically, 0.48 mmol Cd(OAc)$_2$ ·2H$_2$O and 0.8 mmol S were dissolved in 16 mL of C$_2$H$_8$N$_2$ with continuous ultrasound for 20 min and lastly transferred into a 20 mL autoclave, then undergone a 20 h hydrothermal treatment at 200 °C. Subsequently, the harvested CdS NWs was washed and dried at 80 °C for 10 h.

2.6. Preparation of MoNi hierarchical microspheres/CdS nanowires (MoNi HM/CdS NWs) hybrid catalysts

First, 1.0 mg MoNi HM cocatalyst was ultrasonically dispersed in 20 mL D.I. water for 1 h at room temperature. Afterwards, 0.5 mg as-prepared CdS NWs photocatalyst was added to the suspension with continuous ultrasound for 1 h. The obtained suspension ultrasonically dispersed into 80 mL solution containing of 0.35 M Na$_2$SO$_3$ and 0.25 M Na$_2$S in a relatively vacuum system. For comparison, the mass ratios of MoNi HM/CdS NWs = 1.0 mg/0.33 mg (3/1), 1.0 mg/0.5 mg (2/1), 1.0 mg/0.8 mg (5/4), 1.0 mg/1.0 mg (1/1), 0.5 mg/1.0 mg (1/2) were employed.

Details on material characterizations, electrochemical measurements, and photocatalytic measurements were provided in Supporting Information.

3. Results and discussion

The NiMoO$_4$ microspheres were first prepared through a hydrothermal reaction employing MoO$_3$ nanobelts as Mo source and structural regulator (Fig. S1). The MoO$_3$ nanobelts were dissolved by ammonia ions to slowly release Mo ions and then react with Ni ions to form the hierarchical NiMoO$_4$ multilevel microsphere, as shown in Fig. 1a, b. The NiMoO$_4$ microspheres possessing a mean diameter of 1.45 µm were made up of radially oriented nanosheets (Fig. S2a), showing the smooth surface. As a contrast, if using (NH$_4$)$_6$Mo$_7$O$_{24}$·4H$_2$O and Na$_2$MoO$_4$ instead of MoO$_3$ nanobelts, the blocks composed of NiMoO$_4$ without regular morphology were obtained, as shown in Fig. S3, implying the important slow-release action of Mo ions from MoO$_3$ nanobelts. After reduction reaction at 650 °C for 2 h in a H$_2$/Ar gas flow, the microsphere morphology was maintained, while the surface of nanosheets became coarse and porous (Fig. 1c, d), and the sizes of microspheres were slightly decreased (around 1.25 µm) (Fig. S2b). Nitrogen adsorption–desorption isotherms (Fig. 1e) validated the increased specific surface area from 20.46 m^2 g^{-1} of NiMoO$_4$ M to 203.65 m^2 g^{-1} of MoNi HM, due to the porous nanosheets and open porous microspheres. NiMoO$_4$ M possessed open pore structure with pore size distribution of about 34 nm. After reducing reaction, the obtained MoNi HM possessed additional mesoporous with an average diameter of 6 nm (Fig. 1e, inset). The larger surface area as well as the mesoporous structure increased the electrocatalytic sites and promoted mass transfer between electrocatalyst and electrolyte.

XRD pattern in Fig. 1f indicated that the NiMoO$_4$ precursor (JCPDS no. 45-0142) was changed into crystalline phases of the MoNi (JCPDS
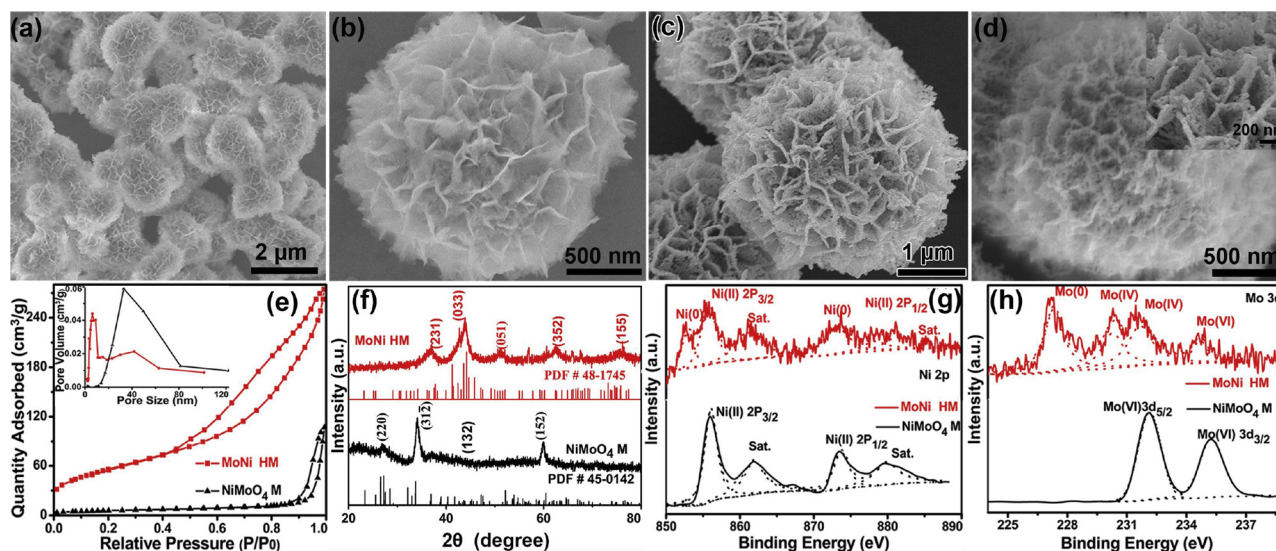
Fig. 1. SEM images of (a, b) NiMoO₄ M and (c, d) MoNi HM, respectively. (e) Nitrogen adsorption/desorption isotherm of NiMoO₄ M and MoNi HM with an inset showing the corresponding pore-size distribution. (f) XRD patterns of NiMoO₄ M and MoNi HM. (g, h) High-resolution XPS spectrums of Ni 2p, Mo 3d on NiMoO₄ M and MoNi HM. Solid curves were experimental data and dashed curves were deconvolution fits.

no. 48-1745) by reduction reaction. The diffraction peaks located at 36.8°, 42.6°, 51.0°, 62.8°, and 75.5° belonged to the (231), (033), (051), (352), and (155) facets of MoNi, respectively. The element compositions and surface chemical environment of NiMoO₄ and MoNi microspheres were performed by XPS analysis. In the fitted XPS Ni 2p region, the peaks at 855.9 eV and 873.8 eV were in accordance with Ni 2p$_{3/2}$ and Ni 2p$_{1/2}$, the peaks at 861.8 eV and 879.6 eV corresponding to their satellite peaks, respectively. The gap in the binding energy between the dominant peaks of Ni 2p$_{3/2}$ and Ni 2p$_{1/2}$ was 17.9 eV, confirming the oxidation state of Ni (II) (the black lines in Fig. 1g). After the reduction to MoNi microsphere, the signal of Ni 2p core level revealed that the dominant peaks were belonged to Ni (0) (852.7 eV, 873.2 eV) and negligible Ni (II) (855.8 eV, 878.5 eV) attribute to the exposure to the air. In the deconvoluted Mo 3d region, the peaks at 231.8 and 234.9 eV, in accordance with Mo 3d$_{3/2}$ and Mo 3d$_{5/2}$, were revealed in the NiMoO₄ M (the black lines in Fig. 1h). As for the Mo 3d region of MoNi HM, the peaks located at 230.2 eV, 232.1 eV, and 234.6 eV belong to Mo (IV) 3d$_{5/2}$, Mo (IV) 3d$_{3/2}$, and Mo (VI) 3d$_{3/2}$, respectively. The Mo (0) 3d$_{5/2}$ were detected at 227.3 eV (the red lines in Fig. 1h) [46]. XPS peaks centered at 227.3 and 852.7 eV corroborated the presence of Mo (0) and Ni (0) on the surface of MoNi HM, respectively.

To investigate the phase transformations and intermediate states formed during the reduction of NiMoO₄ M, an in situ High-Temperature X-ray diffraction (HT-XRD) was carried out every 15 °C from 300 °C to 750 °C and maintained at the desired temperature for 10 min under Ar/H₂ gas flow [47]. The in situ HT-XRD experiments were described in detail in Fig. S4. No noticeable shifts in the diffraction peaks at 52.1° and 56.9° for Al₂O₃ substrate was a reflex from the crucible as internal standards for all HT-XRD patterns. So, the temperature dependent lattice dilatation and forming alloy rather than shift results, for instance, shape change and sintering had an influence on the displacement of reflex. In Fig. 2, only the diffraction peaks at 33.6°, 42.6°, and 59.1° according to (31$\bar{2}$), (132), and (152) of NiMoO₄ could be found below 375 °C. When the temperature increased to above 375 °C, the new diffraction peaks at 42.6° and 65.8° appeared in the diffraction pattern, implying the preferential growth of (033) plane and (352) plane of MoNi. It was worth noting that the (352) plane of MoNi was gradually evolved from the (152) plane of NiMoO₄. At a higher temperature of about 600 °C, the new diffraction peak at 36.8° corresponding to (231) of MoNi started to appear. In total, with increasing temperature, the order in which the crystal faces of MoNi appear was (352), (033) and

(231). To deeply concerned about the extrinsic feature of the (352), (033), and (231) lattice plane, investigated in the XRD pattern of Figs. 1f and 2 b, the neighborhood of the (352), (033) and (231) planes were studied. Fig. 2c showed the measured partial phase gradual transformation from (31 $\bar{2}$) of NiMoO₄ to the (231) lattice plane of MoNi with calcination temperature rising to ∼600 °C. Once the thermal annealing temperature reach to 375 °C and 420 °C, the strong diffraction peak at 2θ = 65.8° and 42.6° that contributed from NiMoO₄ were observed and peak intensity of NiMoO₄ at 2θ = 59.1° and 42.6° were decreased. These results indicated the (033) plane was formed at higher annealing temperature. At an annealing temperature as high as 750 °C the peak intensity of 2θ = 42.6° increased, implying the MoNi was the thermally stable phase (Fig. 2d, e).

To obtain more detailed morphologies and microstructures of the NiMoO₄ M and MoNi HM, the local magnification TEM images were also characterized. NiMoO₄ microsphere consisted of nanosheets possessed an diameter of ∼1.36 μm (Fig. 3a, b). Diffraction rings in the SAED taken from the basal plane of the nanosheets (the inset in Fig. 3b) gave a single crystalline feature with clear diffraction spots. The characteristic spacing of 0.335 nm for the (220) lattice plane of NiMoO₄ was observed in Fig. 3c. Fig. 3d manifested the uniform distribution of elemental Mo, Ni, and O throughout the entire NiMoO₄ M. After a subsequent calcination reduction, MoNi microspheres with multilevel porous structure were transformed from the NiMoO₄ M. The TEM images (Fig. 3e) showed that the microspheres composed of nanosheets remained intact. However, the nanosheets became porous, confirmed by TEM (Fig. 3f). The diffraction rings of (114), (227), (451), (441), (241), and (231) in SAED patterns indicated polycrystalline structure of MoNi HM. The HRTEM image (Fig. 3g) of the porous MoNi nanosheet with a d-spacing of 0.243 nm could be assigned to the (231) lattice plane of MoNi. Noticeably, the EDX results indicated that Mo and Ni elements were homogeneously distributed in the entire microspheres. However, compared with NiMoO₄ M, the oxygen content of MoNi HM was significantly decreased from 58.22 at.% to 6.85 at.%.

The effect of reducing calcining at 450 °C, 550 °C, 650 °C, 750 °C, and 850 °C in porous MoNi alloys on electrocatalytic performance for HER in water electrolysis was investigated (Fig. S5). And the super catalytic capacity of MoNi HM synthesized at optimization reduction temperature of 650 °C may lie in the advantage of the suitable crystal structure (Fig. 2), porous nanosheet morphology (Fig. S6a–d), and largest BET surface area (Fig. S6e, S6f). A three-electrode system was
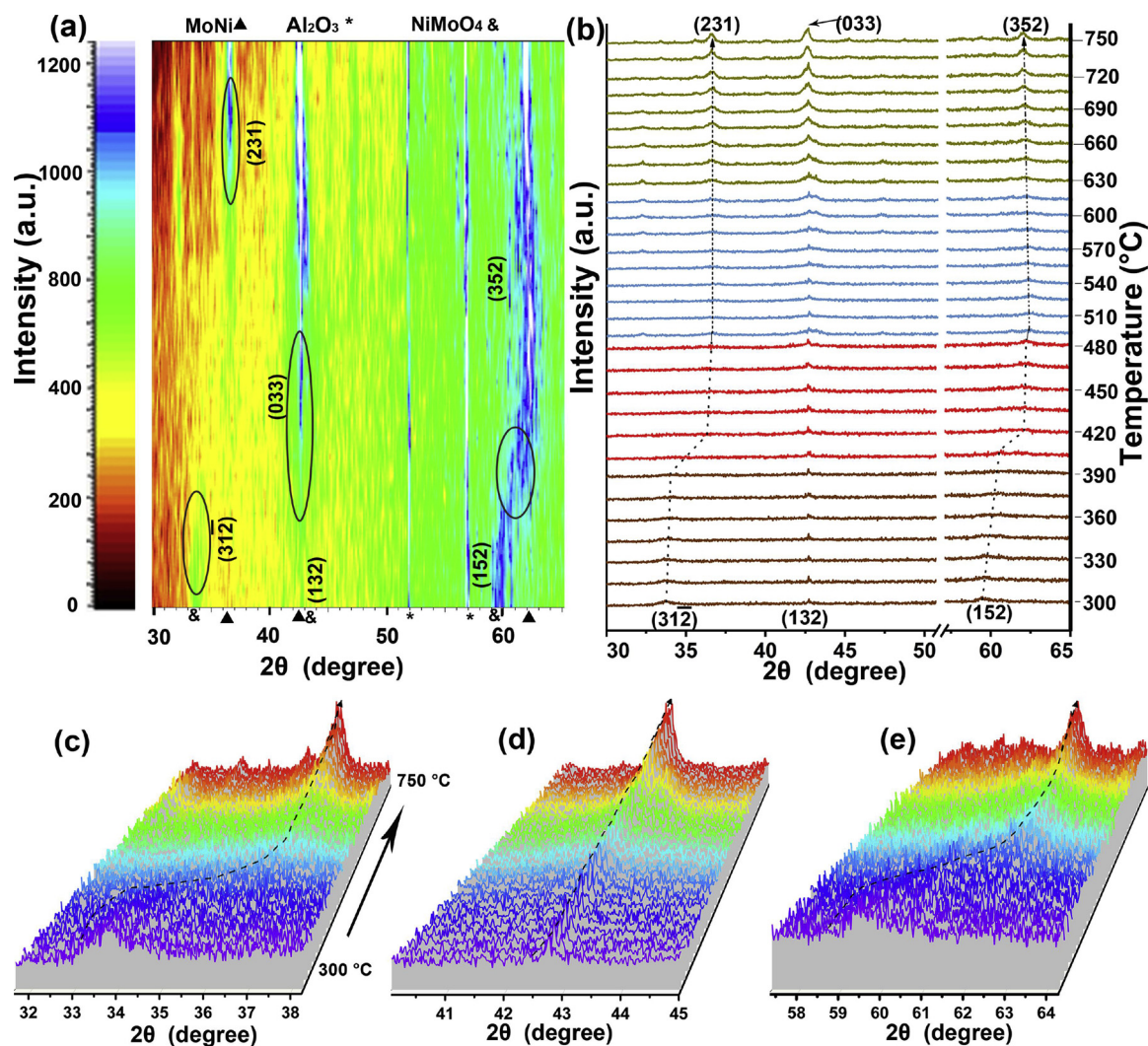
Fig. 2. (a) The image plot of the in situ HT-XRD patterns measured at different temperatures and (b) the corresponding diffraction patterns from (a), (c–e) selected 2θ region plot of the in situ HT-XRD results.
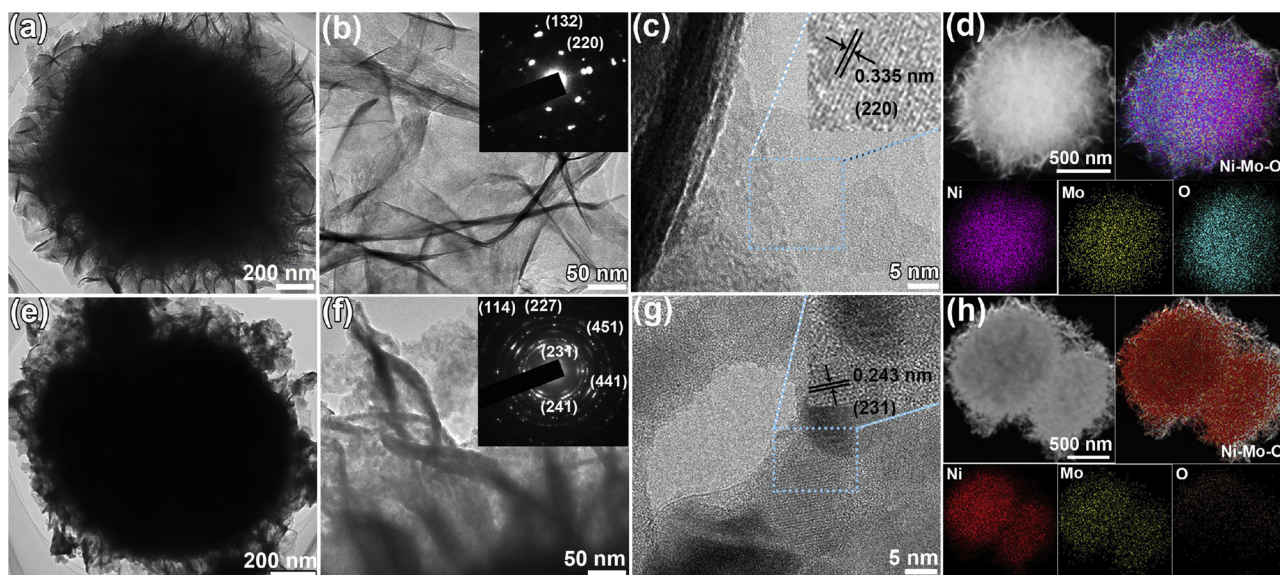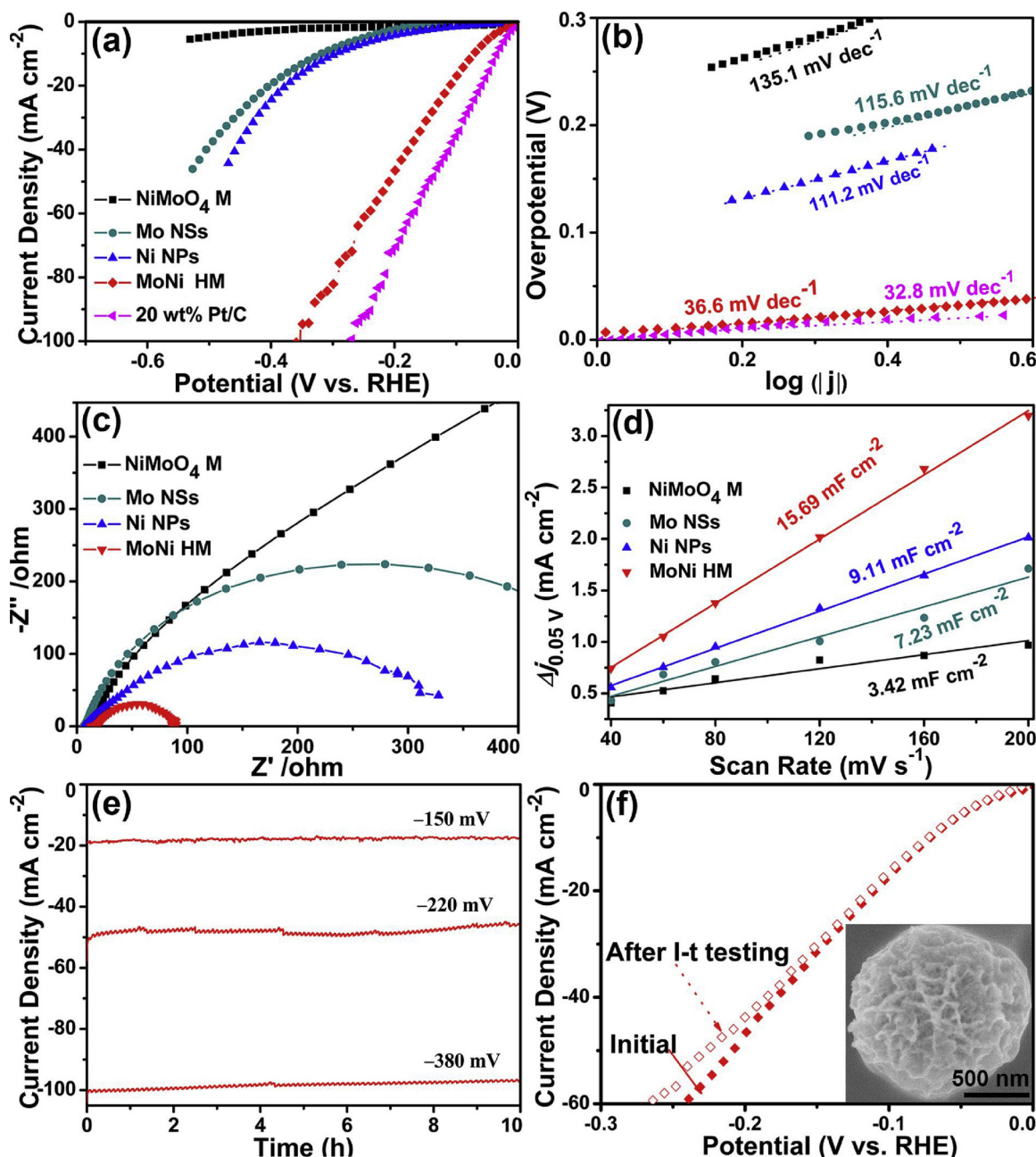

Fig. 3. (HR)TEM and corresponding elemental mapping images of NiMoO₄ M (a–d) and MoNi HM (e–h), the insets in Fig. 3b and f were the related SAED patterns.

Fig. 4. (a) Polarization curves recorded from NiMoO$_4$ M, MoNi HM, Ni nanoparticles (Ni NPs), Mo nanosheets (Mo NSs), and 20 wt% Pt/C catalysts in 1.0 M KOH. (b) Tafel plots of the polarization curves in (a). (c) Electrochemical impedance spectroscopy of NiMoO$_4$ M, Mo NSs, Ni NPs, and MoNi HM at −150 mV vs. RHE. (d) Differences in current density ($\Delta j = j_a − j_c$) at +0.05 V plotted against scan rates. (e) Time-dependent profiles of HER current density on the MoNi at the various applied potential of −150 mV, −220 mV and −380 mV vs. RHE. (f) Polarization curves of MoNi HM before and after long-time HER tests (Inset: SEM image of MoNi HM after HER tests).

utilized to analyze the electrocatalytic HER performances of obtained MoNi HM under basic condition. Some blank samples, including Ni nanoparticles (Ni NPs) and Mo nanosheets (Mo NSs) were prepared, which were concluded from XRD and SEM (Fig. S7). Fig. 4a manifested the polarization curves of NiMoO$_4$ M, MoNi HM, Ni NPs, Mo NSs, and 20 wt% Pt/C with the same mass loading on glassy carbon electrode (GCE). Among these, the precursor NiMoO$_4$ M possessed weak HER property with an onset potential (η_1) of larger than −200 mV vs. RHE (1 mA cm^{-2}). It was worth noting that MoNi HM exhibited an exceptionally low onset potential of −7 mV vs. RHE close to that of 20 wt% Pt/C (−4 mV vs. RHE), which greatly outperformed those of Ni NPs (−101 mV vs. RHE) and Mo NSs (−165 mV vs. RHE). Besides, MoNi HM also possessed the highly HER property in acidic electrolyte, and

showed an onset potential of −11 mV vs. RHE (Fig. S8). However, the clear degradation of current density was recorded from the MoNi HM catalyst, indicating the unstable catalytic activity in acidic solution.

Tafel curves were estimated from the polarization curves to further understand the HER kinetics. As expected, MoNi HM demonstrated the low Tafel slope of 36.6 mV dec^{-1}, close to 20 wt% Pt/C (32.8 mV dec^{-1}), evidently smaller than Ni NPs (111.2 mV dec^{-1}), and Mo NSs (115.6 mV dec^{-1}) (Fig. 4b). A smaller Tafel slope revealed a more favorable HER kinetics and a higher HER speed. On the basis of the classic theory on the catalytic mechanism, the value of 36.6 mV dec^{-1}, indicating the HER mechanism following the Volmer-Heyrovsky step, the corresponding rate-determining step was the H$_2$ electrochemical desorption. Such a HER performance of MoNi HM powder catalyst (onset

potential of -7 mV vs. RHE, Tafel slope of 36.6 mV dec^{-1}, an overpotential (η_{10}) of 72 mV) was outperformed or comparable to those of NiMo-group three-dimension electrodes, e.g. Mo$_{0.6}$Ni$_{0.4}$ alloy nanoparticles-coated-Ti foil (65 mV at current of 10 mA cm^{-2}, 72 mV dec^{-1}) [48], NF/NiMoO-H$_2$ (0 mV, 43 mV dec^{-1}) [49], Ni$_4$Mo nanoclusters/carbon cloth (76 mV at current of 10 mA cm^{-2}, 78 mV dec^{-1}) [50], Ni–Mo nanosheets/Ni foam (–12.5 mV, 45 mV dec^{-1}) [51], NiMo HNRs/Ti mesh (–60 mV, 76 mV dec^{-1}) [26], NC/NiMo/NiMoO$_x$/Ni foam (-5 mV, 46 mV dec^{-1}) [52], MoNi$_4$/MoO$_2$@Ni (0 mV, 30 mV dec^{-1}) [24], Ni–Mo/Cu Nanowire/Cu foam (-77 mV, 107 mV dec^{-1}) [53], Ni–Mo alloy microsphere/copper foils (–12 mV, 49 mV dec^{-1}) [54], porous NiMo (22 mV at current of 10 mA cm^{-2}, 37 mV dec^{-1}) [55] (Table S1).

In Fig. 4c, the EIS analysis was carried out to give insight into the interface reactions. The charge transfer resistance (Rct) obtained from Nyquist plot of the MoNi HM modified-GCE was 89.8 Ω at 150 mV, which was far smaller than that of other samples, such as Ni NPs (320.7 Ω), Mo NSs (514.9 Ω), and NiMoO$_4$ M (> 1000 Ω), indicating that rapid electron diffusion was achieved in MoNi HM, which was associated with the higher catalytic activity. In addition, it could be seen that the Rct values of MoNi HM lowered remarkably as overpotentials augmented, from 322.9 Ω at 50 mV to just 89.8 Ω at 150 mV, implying rapid electron transfer and efficient reaction kinetics (Fig. S9). To further explore the intrinsic catalytic activity of the catalysts, we estimated the turnover frequency (TOF) per active site, which was calculated and plotted against overpotential (Fig. S10). In particular, the TOF values of MoNi HM at 30 and 150 mV (vs. RHE) were 0.16 and 1.73 H$_2$ s^{-1}, respectively.

To elucidate the origin of the highlighted catalytic activity, we performed the cyclic voltammetry tests to investigate the double-layer capacitance (C$_{dl}$), and evaluate the electrochemically effective surface area (ECSA). The ECSA should be improved to promote the HER performance, which was attributed to the nanosheets with porous structure. As shown in Figs. 4d and S11, due to the porous structure, the comparison of C$_{dl}$ values of MoNi HM modified electrode (15.69 m F cm^{-2}) was larger than those of NiMoO$_4$ M (3.42 m F cm^{-2}), Ni NPs (9.11 m F cm^{-2}), and Mo NSs (7.23 m F cm^{-2}). The electrochemically effective surface area results were consistent to the specific surface area (Fig. 1e).

To investigate the stability of MoNi HM in basic solution, the durability test was conducted at -0.15 vs. RHE for 10 h of continuous operations, causing a negligible decline of the current density (Fig. 4e). The periodic fluctuation of Time-dependent profiles of HER current density was ascribed the gather and spilling of generated H$_2$ bubbles. Concerning for the practical application, the larger current densities of ~50 mA cm^{-2} and ~100 mA cm^{-2} carried out at 220 mV and 380 mV respectively for 10 h remained with no obvious attenuation (Fig. 4e). In addition, it could been also seen that the activity of MoNi HM was well-retained with a relatively little decrease of only 2 mV at the current density of 10 mA cm^{-2} after durability testing (Fig. 4f), manifesting prominent durability of the MoNi hierarchical microspheres during hydrogen evolution process in alkaline medium. Furthermore, the inset SEM image of Fig. 4e depicted that the nanosheets structure of the catalyst was well-maintained after the i-t testing, confirming that not only the catalytic durability for HER but also the structure stability of MoNi hierarchical microspheres.

Efficient photocatalytic hydrogen production system required the highly active photocatalyst and the efficient electrocatalyst as cocatalyst. The optimized MoNi HM HER electrocatalysts as cocatalyst to enhance the photocatalytic activity was evaluated by physical mixing MoNi HM and CdS NWs (MoNi HM/CdS NWs). The prepared CdS NWs showed nanowire morphology with diameter ranging from 30 to 70 nm and lengths ranging from 0.5 to 20 μm (Fig. 5a). SEM image in Fig. 5b showed the CdS NWs wrapped around the surface of MoNi HM, and the structure prevented the electrocatalyst from blocking the photocatalyst to absorb light. The XRD and SEM images of CdS NWs and the MoNi

HM/CdS NWs composites mixed mechanically with different MoNi HM/CdS NWs mass ratios were displayed in Fig. S12. The XRD diffraction peaks of bare CdS NWs and MoNi HM/CdS NWs composites could be ascribed to the hexagonal CdS (JCPDS no. 41-1049), without typical peaks of MoNi HM plausibly as a result of the MoNi HM was uniformly wrapped by the CdS NWs, as shown in the SEM images of Figs. 5b and S12a.The UV/vis diffuse reflectance spectroscopy of MoNi HM, pure CdS NWs, and MoNi HM/CdS NWs were shown in Fig. 5c. Pure CdS NWs had a light absorbance at wavelength of around 526 nm, corresponding to the band gap of ~2.18 eV (inset of Fig. 5c). Interestingly, the MoNi HM/CdS NWs sample exhibited a flat plot with an enhancement of light absorbance at wavelength beyond 510 nm, which could be attributed to the stronger photo-absorption of the narrow band and metallic nature of MoNi HM, thus enhanced light harvesting. The calculated bandgap value of MoNi HM/CdS NWs was 1.86 eV indicating that the strong electronic coupling between MoNi HM and their narrower band gaps, thus achieved the enhanced visible-light absorption [41]. The photocurrent measurement was measured to confirm the photoexcited charge separation efficiency and the higher photocurrent intensity resulted in better photocatalytic performance. The MoNi HM/CdS NWs (2:1) composites exhibited the highest transient photocurrent density in comparison with that of MoNi HM and bare CdS NWs, indicating that a higher efficiency of generating transferring the photo-induced charge was held by physical mixing MoNi HM and CdS NW due to more contact interfaces (Fig. 5d). Furthermore, the fitted semicircle diameter based on the EIS Nyquist plots showed that the MoNi HM cocatalyst loading sample afforded highest charge transfer efficiency (Fig. S13), further confirmed the superior charge separation of photo-generated electrons and holes. In addition, compared with that in the dark, the largest change of Rct value for MoNi HM/CdS NWs under light illumination also confirmed the most efficient photocatalytic system.

The photocatalytic H$_2$ evolution of as-synthesized samples was explored as shown in Fig. 5e, f. The pure MoNi HM and CdS NWs displayed poor photocatalytic activities with hydrogen generation rate of 0.6 μmol mg^{-1} h^{-1} and 7.1 μmol mg^{-1} h^{-1}. The MoNi HM/CdS NWs with mass ratio of 2:1 showed the highest hydrogen evolution rate of 151.7 μmol mg^{-1} h^{-1}, a 21.4 times higher than that of pure CdS NWs. Notably, too much or too little MoNi HM cocatalyst resulted in a decrease in H$_2$ generation rate, because excessive MoNi HM would lead to the shield effects and too little cocatalyst was insufficient to offer adequate photocatalytic reaction sites [56]. The photocatalytic stability of the MoNi HM/CdS NWs (2:1) photocatalyst was also conducted at three consecutive hydrogen production cycles. As displayed in Fig. S14a, no significant deterioration in activity was observed, suggesting that MoNi HM/CdS NWs was a stable photocatalyst for photocatalytic hydrogen production. These above results demonstrated that suitable content of MoNi HM and CdS NWs could not only improved the optical absorption ability but also facilitated electron-hole separation efficiency, eventually contributing to the outstanding photocatalytic H$_2$ generation activity of the MoNi HM/CdS NWs. For the sake of studying the advantages brought by MoNi HM, a series of experiments had been carried out. Likewise, the apparent quantum efficiency (AQE) values as a function of the incident light wavelengths were illustrated in Fig. S14b, finding across its optical absorption spectrum. Increasing wavelength tended to decrease AQE as the photon potential decreased, and the longest wavelength at 520 nm (close to absorption edge) was still capable of inducing water splitting with an AQE value of 3.5% [44,57].

4. Conclusions

In this research, we reported a novel strategy for synthesizing uniform hierarchical microspheres composed of porous MoNi nanosheets (MoNi HM) structure from the NiMoO$_4$ microspheres precursor. The obtained MoNi HM at optimized calcining temperature of 650 °C with suitable crystal structure, porous nanosheet morphology and large BET surface area could enhance intrinsic catalytic activity, which displayed
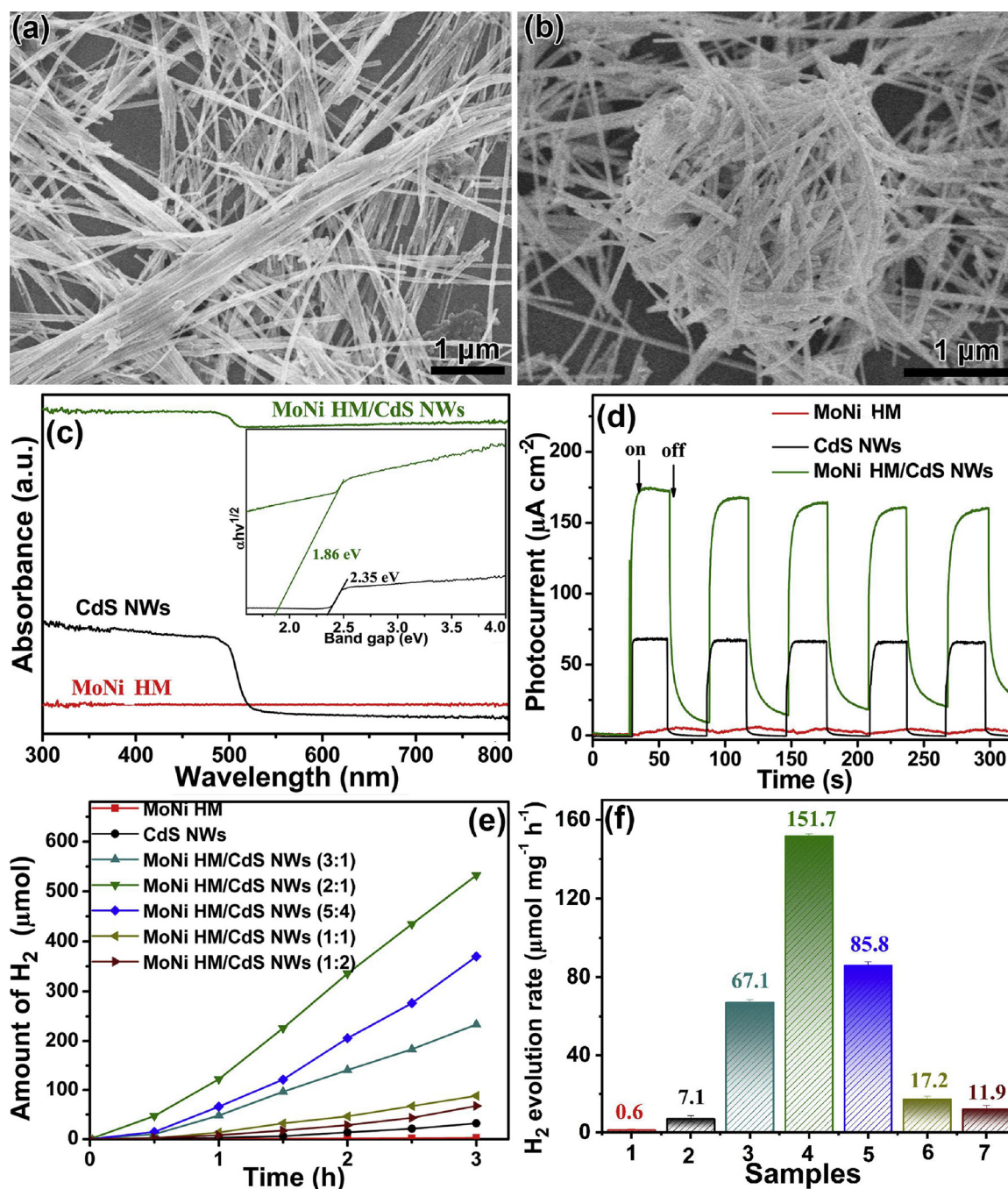
Fig. 5. SEM images of (a) pure CdS NWs and (b) MoNi HM/CdS NWs, (c) UV/Vis diffuse reflectance spectra with the calculated bandgap values (Inset) and (d) Photocurrent responses of MoNi HM, CdS NWs, and MoNi HM/CdS NWs. (e) Time-dependent photocatalytic H_2 evolution and (f) Average photocatalytic H_2 production rates over pure CdS NWs, MoNi HM, MoNi HM/CdS NWs (3:1), MoNi HM/CdS NWs (2:1), MoNi HM/CdS NWs (5:4), MoNi HM/CdS NWs (1:1), and MoNi HM/CdS NWs (1:2).

a onset potential of -7 mV vs. RHE and a low Tafel slope of 36.6 mV per dec^{-1} in 1.0 M KOH. Furthermore, MoNi HM as cocatalyst and CdS NWs as photocatalyst were physically mixed to fast and simply construct the photocatalytic system (MoNi HM/CdS NWs). The porous nanosheet of MoNi and nanowire of CdS promoted the separation of photogenerated electron-hole pairs due to more contact interfaces. The MoNi HM/CdS NWs nanocomposite presented a record-high photocatalytic activity for H_2 evolution with an excellent hydrogen evolution rate of 151.7 μmol mg^{-1} h^{-1}, which was 21.4-fold superior than that of CdS NWs alone under visible light irradiation. This study revealed a process for building highly efficient electrocatalyst and cocatalyst with multi-structure to enhance the electro- and photo-catalytic H_2 evolution.

Appendix A. Supplementary data

Supplementary material related to this article can be found, in the online version, at doi:https://doi.org/10.1016/j.apcatb.2019.02.062.

References

[1] S. Pacala, R. Socolow, Science 305 (2004) 968–972.
[2] H. Jiang, D. Ren, H. Wang, Y. Hu, S. Guo, H. Yuan, P. Hu, L. Zhang, C. Li, Adv. Mater 27 (2015) 3687–3695.
[3] X. Zou, Y. Zhang, Chem. Soc. Rev. 44 (2015) 5148–5180.
[4] J. Jia, T. Xiong, L. Zhao, F. Wang, H. Liu, R. Hu, J. Zhou, W. Zhou, S. Chen, ACS Nano 11 (2017) 12509–12518.
[5] W. Zhou, J. Jia, J. Lu, L. Yang, D. Hou, G. Li, S. Chen, Nano Energy 28 (2016) 29–43.
[6] R. Subbaraman, D. Tripkovic, D. Strmcnik, K.-C. Chang, M. Uchimura, A.P. Paulikas, V. Stamenkovic, N.M. Markovic, Science 334 (2011) 1256–1260.
[7] P. Wang, X. Zhang, J. Zhang, S. Wan, S. Guo, G. Lu, J. Yao, X. Huang, Nat. Commun. 8 (2017) 14580.
[8] L. Zhang, L. Han, H. Liu, X. Liu, J. Luo, Angew. Chem. Int. Ed. 56 (2017) 13900–13900.
[9] I.E.L. Stephens, I. Chorkendorff, Angew. Chem. Int. Ed. 50 (2011) 1476–1477.
[10] L. Yang, W. Zhou, J. Lu, D. Hou, Y. Ke, G. Li, Z. Tang, X. Kang, S. Chen, Nano Energy 22 (2016) 490–498.
[11] J.M. Woods, Y. Jung, Y. Xie, W. Liu, Y. Liu, H. Wang, J.J. Cha, ACS Nano 10 (2016) 2004–2009.
[12] C. Tang, N. Cheng, Z. Pu, W. Xing, X. Sun, Angew. Chem. Int. Ed. 127 (2015) 9483–9487.
[13] Y. Ji, L. Yang, X. Ren, G. Cui, X. Xiong, X. Sun, ACS Sustain, J. Mater. Chem. A 6 (2018) 9555–9559.
[14] J. Zhao, X. Li, G. Cui, X. Sun, Chem. Commun. 54 (2018) 5462–5465.
[15] C. Tang, R. Zhang, W. Lu, L. He, X. Jiang, A.M. Asiri, X. Sun, Adv. Mater 29 (2017) 1602441.
[16] X. Fan, Y. Liu, Z. Peng, Z. Zhang, H. Zhou, X. Zhang, B.I. Yakobson, W.A. Goddard, X. Guo, R.H. Hauge, J.M. Tour, ACS Nano 11 (2017) 384–394.
[17] C. Lu, D. Tranca, J. Zhang, Fn. Rodríguez Hernández, Y. Su, X. Zhuang, F. Zhang, G. Seifert, X. Feng, ACS Nano 11 (2017) 3933–3942.
[18] L. Yang, W. Zhou, J. Jia, T. Xiong, K. Zhou, C. Feng, J. Zhou, Z. Tang, S. Chen, Carbon 122 (2017) 710–717.
[19] W. Zhou, T. Xiong, C. Shi, J. Zhou, K. Zhou, N. Zhu, L. Li, Z. Tang, S. Chen, Angew. Chem. Int. Ed. 128 (2016) 8556–8560.
[20] W. Zhou, J. Zhou, Y. Zhou, J. Lu, K. Zhou, L. Yang, Z. Tang, L. Li, S. Chen, Chem. Mater. 27 (2015) 2026–2032.
[21] J.R. McKone, B.F. Sadtler, C.A. Werlang, N.S. Lewis, H.B. Gray, ACS Catal. 3 (2013) 166–169.
[22] T. Wang, Y. Guo, Z. Zhou, X. Chang, J. Zheng, X. Li, ACS Nano 10 (2016) 10397–10403.
[23] M. Fang, W. Gao, G. Dong, Z. Xia, S. Yip, Y. Qin, Y. Qu, J.C. Ho, Nano Energy 27 (2016) 247–254.
[24] J. Zhang, T. Wang, P. Liu, Z. Liao, S. Liu, X. Zhuang, M. Chen, E. Zschech, X. Feng, Nat. Commun. 8 (2017) 15437.
[25] Y.-Y. Chen, Y. Zhang, X. Zhang, T. Tang, H. Luo, S. Niu, Z.-H. Dai, L.-J. Wan, J.-S. Hu, Adv. Mater 29 (2017) 1703311.
[26] J. Tian, N. Cheng, Q. Liu, X. Sun, Y. He, A.M. Asiri, J. Mater. Chem. A 3 (2015) 20056–20059.
[27] C.C.L. McCrory, S. Jung, I.M. Ferrer, S.M. Chatman, J.C. Peters, T.F. Jaramillo, J. Am. Chem. Soc. 137 (2015) 4347–4357.
[28] I.A. Raj, K.I. Vasu, J. Appl. Electrochem. 20 (1990) 32–38.
[29] R. Subbaraman, D. Tripkovic, K.-C. Chang, D. Strmcnik, A.P. Paulikas, P. Hirunsit, M. Chan, J. Greeley, V. Stamenkovic, N.M. Markovic, Nat. Mater. 11 (2012) 550.
[30] J. Zhang, Z. Yu, Z. Gao, H. Ge, S. Zhao, C. Chen, S. Chen, X. Tong, M. Wang, Z. Zheng, Y. Qin, Angew. Chem. Int. Ed. 56 (2017) 816–820.
[31] L. Zhao, J. Jia, Z. Yang, J. Yu, A. Wang, Y. Sang, W. Zhou, H. Liu, Appl. Cataly. B: Environ. 210 (2017) 290–296.
[32] H. He, J. Lin, W. Fu, X. Wang, H. Wang, Q. Zeng, Q. Gu, Y. Li, C. Yan, B.K. Tay, C. Xue, X. Hu, S.T. Pantelides, W. Zhou, Z. Liu, Adv. Energy Mater. 6 (2016) 1600464.
[33] X. Zong, H. Yan, G. Wu, G. Ma, F. Wen, L. Wang, C. Li, J. Am. Chem. Soc. 130 (2008) 7176–7177.
[34] W. Zhou, Z. Yin, Y. Du, X. Huang, Z. Zeng, Z. Fan, H. Liu, J. Wang, H. Zhang, Small 9 (2013) 140–147.
[35] M.-C. Hsiao, C.-Y. Chang, L.-J. Niu, F. Bai, L.-J. Li, H.-H. Shen, J.-Y. Lin, T.-W. Lin, J. Power Sources 345 (2017) 156–164.
[36] J. Zhang, W. Yao, C. Huang, P. Shi, Q. Xu, J. Mater. Chem. A 5 (2017) 12513–12519.
[37] Z. Huang, Z. Chen, Z. Chen, C. Lv, H. Meng, C. Zhang, ACS Nano 8 (2014) 8121–8129.
[38] A. Indra, A. Acharjya, P.W. Menezes, C. Merschjann, D. Hollmann, M. Schwarze, M. Aktas, A. Friedrich, S. Lochbrunner, A. Thomas, M. Driess, Angew. Chem. Int. Ed. 56 (2017) 1653–1657.
[39] L. Li, Z. Deng, L. Yu, Z. Lin, W. Wang, G. Yang, Nano Energy 27 (2016) 103–113.
[40] W. Zhen, H. Gao, B. Tian, J. Ma, G. Lu, ACS Appl. Mater. Interfaces 8 (2016) 10808–10819.
[41] S. Ma, Y. Deng, J. Xie, K. He, W. Liu, X. Chen, X. Li, Appl. Cataly. B: Environ. 227 (2018) 218–228.
[42] K. Chang, X. Hai, J. Ye, Adv. Energy Mater. 6 (2016) 1502555.
[43] J. Ran, J. Zhang, J. Yu, M. Jaroniec, S.Z. Qiao, Chem. Soc. Rev. 43 (2014) 7787–7812.
[44] X. Han, D. Xu, L. An, C. Hou, Y. Li, Q. Zhang, H. Wang, Appl. Cataly. B: Environ. 243 (2019) 136–144.
[45] S. Guan, X. Fu, Y. Zhang, Z. Peng, Chem. Sci. 9 (2018) 1574–1585.
[46] Y. Jin, X. Yue, C. Shu, S. Huang, P.K. Shen, J. Mater. Chem. A 5 (2017) 2508–2513.
[47] C. Ling, J. Hao, J. Haibo, G. Haoxuan, G. Shaojun, H. Yanjie, L. Chunzhong, Adv. Energy Mater. 7 (2017) 1602782.
[48] T. Zhang, X. Liu, X. Cui, M. Chen, S. Liu, B. Geng, Adv. Mater. Interfaces 5 (2018) 1870063.
[49] Z.-Y. Yu, C.-C. Lang, M.-R. Gao, Y. Chen, Q.-Q. Fu, Y. Duan, S.-H. Yu, Energy Environ. Sci. 11 (2018) 1890–1897.
[50] Y. Zhang, B. Ouyang, K. Xu, X. Xia, Z. Zhang, R.S. Rawat, H.J. Fan, Small 14 (2018) 1800340.
[51] Q. Zhang, P. Li, D. Zhou, Z. Chang, Y. Kuang, X. Sun, Small 13 (2017) 1701648.
[52] J. Hou, J. Wu, S. Cao, Y. Sun, L. Sun, Small 13 (2017) 1702018.
[53] S. Zhao, J. Huang, Y. Liu, J. Shen, H. Wang, X. Yang, Y. Zhu, C. Li, J. Mater. Chem. A 5 (2017) 4207–4214.
[54] M.Y. Gao, C. Yang, Q.B. Zhang, J.R. Zeng, X.T. Li, Y.X. Hua, C.Y. Xu, P. Dong, J. Mater. Chem. A 5 (2017) 5797–5805.
[55] Y. Ito, T. Ohto, D. Hojo, M. Wakisaka, Y. Nagata, L. Chen, K. Hu, M. Izumi, J.-i. Fujita, T. Adschiri, ACS Catal. 8 (2018) 3579–3586.
[56] Q. Li, B. Guo, J. Yu, J. Ran, B. Zhang, H. Yan, J.R. Gong, J. Am. Chem. Soc. 133 (2011) 10878–10884.
[57] C. Zhu, Ca. Liu, Y. Fu, J. Gao, H. Huang, Y. Liu, Z. Kang, Appl. Cataly. B: Environ. 242 (2019) 178–185.